Bio-Templated Chiral Zeolitic Imidazolate Framework-8 for Enantioselective Chemoresistive Sensing

Minkyu Kim,[a] Moon Jong Han,[a] Hansol Lee,[a] Paraskevi Flouda,[a] Daria Bukharina,[a] Kellina J. Pierce,[a] Katarina M. Adstedt,[a] Madeline L. Buxton,[a] Young Hee Yoon,[b] William T. Heller,[c] Srikanth Singamaneni,[d] Vladimir V. Tsukruk[a]*

[a] School of Materials Science & Engineering, Georgia Institute of Technology, Atlanta, GA 30332, USA

[b] School of Chemical & Biomolecular Engineering, Georgia Institute of Technology, Atlanta, Georgia 30332, USA

[c] Neutron Scattering Division, Oak Ridge National Laboratory, Oak Ridge, Tennessee 37831, USA

[d] Department of Mechanical Engineering and Materials Science, Institute of Materials Science and Engineering, Washington University in St. Louis, St Louis, Missouri, 63130, USA

* Corresponding Author E-mail: vladimir@mse.gatech.edu, Phone: 404-894-6081.

Abstract

Chiral metal-organic frameworks (MOFs) have gained rising attention as ordered nanoporous materials for enantiomer separations, chiral catalysis, and sensing. Among those, chiral MOFs are generally obtained through complex synthetic routes by using a limited choice of reactive chiral organic precursors as the primary linkers or auxiliary ligands. Here, we report a template-controlled synthesis of chiral MOFs from achiral precursors grown on chiral nematic cellulose-derived nanostructured bio-templates. We demonstrate that chiral MOFs, specifically, zeolitic imidazolate framework-8 (ZIF-8), can be grown from regular precursors within nanoporous organized chiral nematic nanocelluloses *via* directed assembly on twisted bundles of cellulose nanocrystals. The template-grown chiral ZIF-8 possesses tetragonal crystal structure with chiral space group of $P4_1$, which is different from traditional cubic crystal structure of $I\text{-}43m$ for freely grown conventional ZIF-8. The uniaxially compressed dimensions of the unit cell of templated ZIF-8 and crystalline dimensions are signatures of this structure. We observe that the templated chiral ZIF-8 can facilitate the enantiotropic sensing. It shows enantioselective recognition and chiral sensing abilities with a low limit of detection of 39 μM and the corresponding limit of chiral detection of 300 μM for representative chiral amino acid, D- and L- alanine.

Introduction

The development of materials for next-generation biomedical sensors, quantum information, and energy storage is a leading driving force of the new era. Chiral materials such as chiral metal-organic frameworks (MOFs) have been rarely demonstrated despite their potentially fascinating properties. MOFs are promising porous and organized materials for energy and gas storage, separation membranes, drug delivery, catalysis, sensors, and bio-preservation.[1,2,3,4,5,6,7] These organic–inorganic hybrids have garnered wide attention owing to their high porosity, designable topologies, and rich chemical functionality.

Control of material's chirality is pivotal in a wide range of fields from chemistry to physics and biology.[8,9] Chiral organic materials have been extensively studied since the first discovery of molecular chirality by Louis Pasteur.[10,11] Recently, there has been a burgeoning interest in chiral organic-inorganic hybrids owing to their unique physical properties.[11] The preservation and extension of chirality from the molecular and nanoscale scales to micro/macroscopic scales in biology still remains elusive. In nature, there are many hierarchical chiral structures, such as exoskeletons of beetles (e.g., *Chrysina gloriosa*)[12] and crustaceans[13], all of which show homochirality.[14] The origin of homochirality in nature has been recognized as one of the 125 most compelling questions thus far, noted by *Science* magazine.[15] One of the critical challenges in preparing chiral MOFs is synthesizing novel chiral structures from achiral building blocks and achieving homochirality.[16,17] Typically, chiral MOFs are assembled from chiral molecular building blocks. The general route to synthesizing chiral MOFs is using chiral organic molecules as one of the primary linkers or auxiliary ligands as depicted in Figure 1a (left arrow).[16] However, this method has a significant drawback in that, mostly, expensive and privileged chiral building blocks are required from a limited pool of chiral building blocks.[16,18]

In contrast, synthesizing chiral MOFs from achiral precursors, illustrated in Figure 1a (right arrow), possesses the advantages of overcoming the generally established method: higher availability of abundant achiral precursors, synthetic simplicity, and mostly, lower cost.[16,18] MOFs have been subjected to diverse crystal structure engineering through various methods.[2,19]. In some cases, chirality is transferred into the MOF *via* a chiral additive or chiral solvent environment, which mostly employs synthetic chiral reagents that require complicated synthetic steps thus resulting in limited and retarded development of chiral MOFs.[16,18] It has been shown that biomacromolecules

can directly initiate the crystallization of MOFs.[20,21] Additionally, Che and co-workers demonstrated that chiral lipid fiber template can transfer chirality to the achiral precursor of TiO_2, enabling synthesis of chiral TiO_2 from the achiral precursor.[22] Accordingly, we envision that if naturally abundant and sustainable biologically chiral materials such as cellulose nanocrystals (CNCs) can transfer chirality to achiral materials, this can bring exponential generations of chiral MOFs by replacing traditionally employed synthetic chiral reagents. Novel synthesis methods to realize chiral MOFs materials from achiral building blocks will facilitate scalable chiral porous organized materials enantiomer separations, catalysis, and sensors.[16,17] Despite MOF-CNC composites have been reported,[23,24] chirality of the MOFs in the composites has not investigated to date.

Here, we report scalable and effective methods for achieving chiral MOFs from achiral precursors by using nanocellulose materials, abundant and sustainable biopolymers. We anticipate that this strategy will exponentially generate chiral MOFs, followed by their effective usage in diverse applications such as enantiotropic biomedical sensors. In this study, chiral zeolitic imidazolate framework-8 (ZIF-8) MOF is synthesized from achiral building blocks by utilizing chiral nematic organization of CNCs as hierarchical bio-templates for growth of MOFs from infiltrated precursors (Figure 1). CNC materials chosen as bio-templates possess three-levels of chirality: i) molecular level: asymmetric carbon atoms of D-glucose unit; ii) nanoscale: spindle-shaped individual nanocrystals; and iii) macroscale: left-handed chiral nematic liquid crystal organization.[25,26,27,28] Overall, template-grown ZIF-8 reported here displays anisotropic shapes and a chiral tetragonal unit cell with $a = b = 12.1$ Å, $c = 8.6$ Å, $\alpha = \beta = \gamma = 90^{o}$, and the $P4_1$ chiral space group. It possesses high specific surface area of 828 m^2/g, having both fine nanopores ($d < 2$ nm) and greatly expanded mesopore content (dimensions $2 < d < 50$ nm) due to the removal of dominating CNCs (83 wt.%) from the chiral CNC-ZIF-8 composite. Moreover, chiral ZIF-8 shows strong positive circular dichroism and selective recognition ability, which facilitates active enantioselective ability for fabricated field-effect chemoresistive sensor. Very high enantioselective recognition and chiral sensing abilities are characterized by a low limit of detection (LOD) of 39 μM and a limit of chiral detection (LOCD) of 300 μM for representative chiral amino acid, L- and D- alanine.

Results and Discussion

To verify the central synthetic hypothesis, achiral precursors of ZIF-8, zinc nitrate and 2-methyl

imidazole, were infiltrated and reacted in a porous, chiral nematic CNC film with well-developed helicoidal twisted organization with nanoscale pitch length (Figure 1b). Specifically, the precursors are infiltrated into the CNC film using vacuum filtration, followed by their growth in the swollen state (see Methods). It has been shown that diverse molecules can be adsorbed on the chiral CNC surface *via* hydrogen bonding, including amine-containing molecules and silicates.[27,29,30,31] Since there are a large number of hydrogen bonding donors and acceptors in the chiral CNCs, especially the D-glucose unit, it is possible for 2-methyl imidazole to asymmetrically interact with the chiral D-glucose unit of CNC *via* multiple hydrogen bonding. The asymmetrically arranged 2-methyl imidazole on the surface of CNC could be propagated and preserved due to the sandwiched CNC structure in the self-assembled chiral nematic structured CNCs. At the same time, it has been demonstrated that chiral MOFs can be synthesized from achiral precursors using chiral induction additives that are not incorporated in the chiral MOF products. Regarding this phenomenon, it has been proposed that the asymmetric crystallization of achiral precursors is originated from the cooperative interactions between chiral induction additives and achiral precursors.[17,18,32,33,34] Specifically, organic chiral induction additives can coordinate with metal precursor and can participate in the nucleation, enabling the control of the chirality of the MOFs.

Our ZIF-8-CNC composite shows the S-O peak shift from 816 cm^{-1} of pristine CNC to 810 cm^{-1}, indicating interaction happens between the S-O group of CNC with ZIF-8. Thus, we can infer that the possible coordination S-O group of chiral D-glucose in CNC between Zn ion provides different coordination geometry for Zn compared to Zn only coordinated with 2-methyl imidazole. Overall, we suggest that newly introduced coordination geometry for Zn and the asymmetrically positioned 2-methyl imidazole by chiral D-glucose of CNC lead to formation of chiral ZIF-8 (Figure 1c).

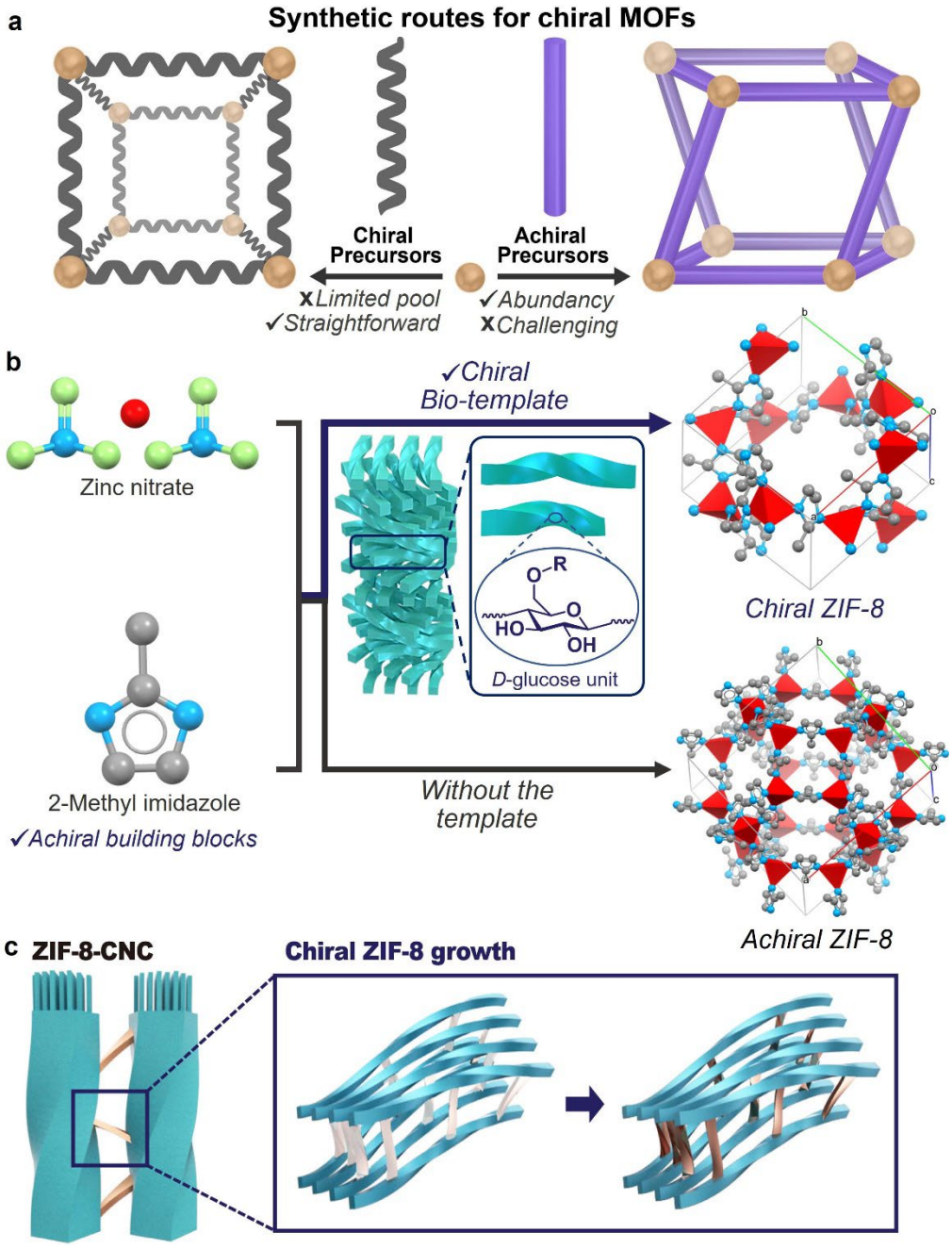

Figure 1. Templated ZIF-8 synthesis. a) Synthetic routes for chiral MOFs from i) chiral precursors and ii) achiral precursors. b) Schematic strategy to produce templated ZIF-8. The -OR is the sulfate group in this research. Green: oxygen, blue: nitrogen, red: zinc, and grey: carbon. c) Chiral ZIF-8 growth from achiral precursors in confined twisted geometry of chiral bio-template and on the chiral surface group. Pale and semi-transparent gold color in the middle of the scheme represents the possible asymmetrically arranged 2-methyl imidazole between the twisted CNCs with chiral D-glucose unit and coordinated Zn ions with S-O group of chiral D-glucose of CNC which provides different coordination geometry for Zn compared to Zn only coordinated with 2-methyl imidazole.

Firstly, we observed that the needle-like structured ZIF-8-CNCs maintained the original chiral organization of CNCs (Figures 2a and 2b). Importantly, the high-resolution scanning electron microscopy (HR-SEM) and transmission electron microscopy (TEM) images of the ZIF-8-CNCs in Figures 2b and 2e show their larger diameter of 40.0 ± 28.0 nm in contrast to the cellulose nanocrystals whose diameter is 5.6 ± 0.6 nm was measured with the atomic force microscopy (AFM) (Figures 2d and S10).

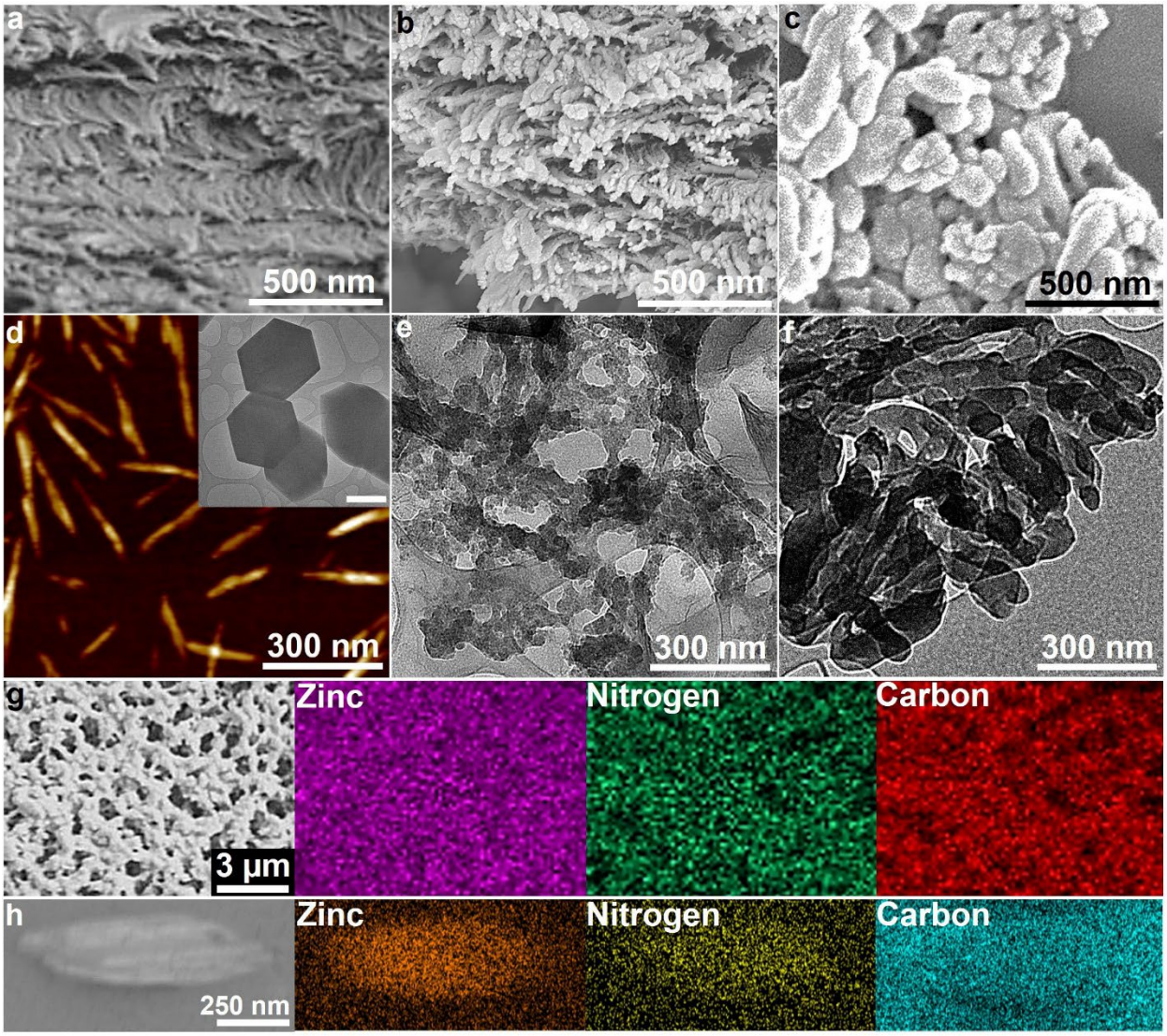

Figure 2. Structure of templated ZIF-8. a-c) SEM images of CNC film, ZIF-8-CNC film, and templated ZIF-8, respectively. d) HR-AFM image of CNC with 12 nm Z-scale of (inset: TEM of ZIF-8. Scale bar: 500 nm). e, f) TEM image of ZIF-8-CNC and templated ZIF-8, respectively. g, h) Energy dispersive X-ray spectroscopy (EDX) mapping of templated ZIF-8: g) aggregated templated ZIF-8 and h) a bundle of templated ZIF-8.

Next, pure templated-grown ZIF-8 can be separated after full removal of the CNCs with *N*-methyl morpholine *N*-oxide monohydrate (NMMO·H_2O) from the ZIF-8-CNC film (Figures S4 and S5).[35,36] It was reported that ZIF-8 shows high chemical stability toward the nitroxide compound.[37] Taking this fact into account, we can deduce that structure of chiral ZIF-8 after full removal of CNCs with nitroxide compound, NMMO·H_2O, would be same with that of ZIF-8 in the composite film. As can be seen in Figures 2c, 2f to 2h, S9, and S10, the templated grown ZIF-8 has a needle-like morphology with a broad distribution of diameters and lengths around 84 nm and 270 nm, respectively. We propose that the enlarged diameter of templated ZIF-8 is due to the aggregation of ZIF-8 nanocrystals during the CNC removal process. Additionally, templated ZIF-8 displays four-time increased mesopore volume than ZIF-8 with negligible difference in nanopore volume (effective dimensions of around 2 nm) (Figures S9, S12, and Table S1).

The morphology of the templated ZIF-8 is different from freely grown ZIF-8s that have the typical rhombic dodecahedral shape with a diameter of 1100 nm (Figures 2d inset and S11).[38] Furthermore, EDX mapping images of the needle-like structured ZIF-8-CNC composite show a uniform distribution of zinc and nitrogen across the entire volume (Figure S1). Additionally, the characteristic Zn-N peak of ZIF-8 in ZIF-8-CNC composite shows at 420 cm^{-1} in attenuated total reflectance Fourier transform infrared spectra (ATR FTIR) that confirms the formation of ZIF-8 in the composite (Figure S2). The blue shift of the SO_3^- peak of CNCs indicates an ion interaction between CNC and ZIF-8 (Figure S2C). Moreover, thermogravimetric analysis (TGA) data shows that 17 wt.% of ZIF-8 is present in the ZIF-8-CNC materials (Figure S3).

The solid-state ^{13}C cross-polarization magic angle spinning nuclear magnetic resonance (^{13}C CP/MAS NMR) spectrum in Figure S6 displays that both templated ZIF-8 and freely grown ZIF-8 present characteristic resonances of ZIF-8. ^{13}C NMR of templated-grown ZIF-8 and conventional achiral ZIF-8 show the carbon peak position difference of 2-methyl imidazole-organic ligand each other (Figure S). ^{13}C NMR has been widely utilized for identifying chiral materials.[39,40] For instance, when the carbon atoms are positioned at different stereo environments, such as in a diastereoisomeric complex composed of i) one enantiomer (*e.g.*, *S*) or ii) another enantiomer (*e.g.*, *R*), they show the carbon peak position difference,[40] for instance, carbon peak position difference from 0.01 to 0.3 ppm for chiral solvating agents.[39] Therefore, the observed carbon peak position difference between templated-grown ZIF-8 and conventional ZIF-8 indicates that carbon atoms in

templated-grown ZIF-8 are positioned differently than in conventional achiral ZIF-8 due to the different unit cell symmetry (see Figure 3 and below).

Additionally, there are no characteristic CNC peaks in the templated ZIF-8, showing the successful complete removal of the CNC component (Figure S6).[41,42] X-ray photoelectron spectroscopy (XPS) confirms that the carbon/nitrogen atomic percentage ratio of the extracted, templated ZIF-8 is identical to freely grown ZIF-8 (Figures S7 and S8).[43,44,45] Furthermore, EDX mapping of the templated ZIF-8 demonstrates a homogeneous distribution of zinc and nitrogen atoms across the specimen (Figures 2g and 2h). Overall, these chemical compositional analyses confirm the removal of CNC from the ZIF-8-CNC composite and, thus, the formation of pure templated ZIF-8 material free of traces of the original bio-template.

X-ray diffraction (XRD) analysis for the ZIF-8-CNC composite reveals a series of sharp and overlapped diffuse peaks in the range from 5 to 40º (Figure 3a). Three intense diffuse peaks around 15º, 16º, and 22º for ZIF-8-CNC composite materials confirm the presence of small diameter one-dimensional (1D) cellulose nanocrystals with parameters of the unit cell of cellulose backbones with a = 7.78 Å, b = 8.20 Å, c = 10.38 Å, and α = β = 90º and γ = 96.5º (Figure 3a and Table S2).[46,47,48] In control XRD measurements, we confirmed that the positions and intensities of the sharp peaks in common ZIF-8 are consistent with a space group of *I*-43m with the unit cell parameters a = b = c = 17.0 Å and α = β = γ = 90º, as expected for traditional cubic structure for this compound (Figures 3c, 3e, Tables S3, S4).[49,50]

Next, we extracted the templated ZIF-8 in order to determine the crystalline structure.[51] Complete disappearance of the diffuse CNC peaks in final templated ZIF-8 materials after hydrothermal treatment further confirms NMR results (Figure S6**)** and XPS data (Figure S7) on complete removal of cellulose nanocrystals during the post-treatment. XRD data for templated ZIF-8 follow a similar pattern but with minor shifts in peak positions and a significant redistribution of intensities of primary peaks (Figure 3b and Table S3). These changes indicate a significant reorganization in the crystal structure of ZIF-8 crystals grown within CNC templates.

Indeed, the crystal structure of templated ZIF-8 is best fit with a chiral space group of $P4_1$ and tetragonal unit cell with different dimensions: a = b = 12.1 Å and c = 8.6 Å and α = β = γ = 90º (Figures 3d, 3f, Tables S3, S4).

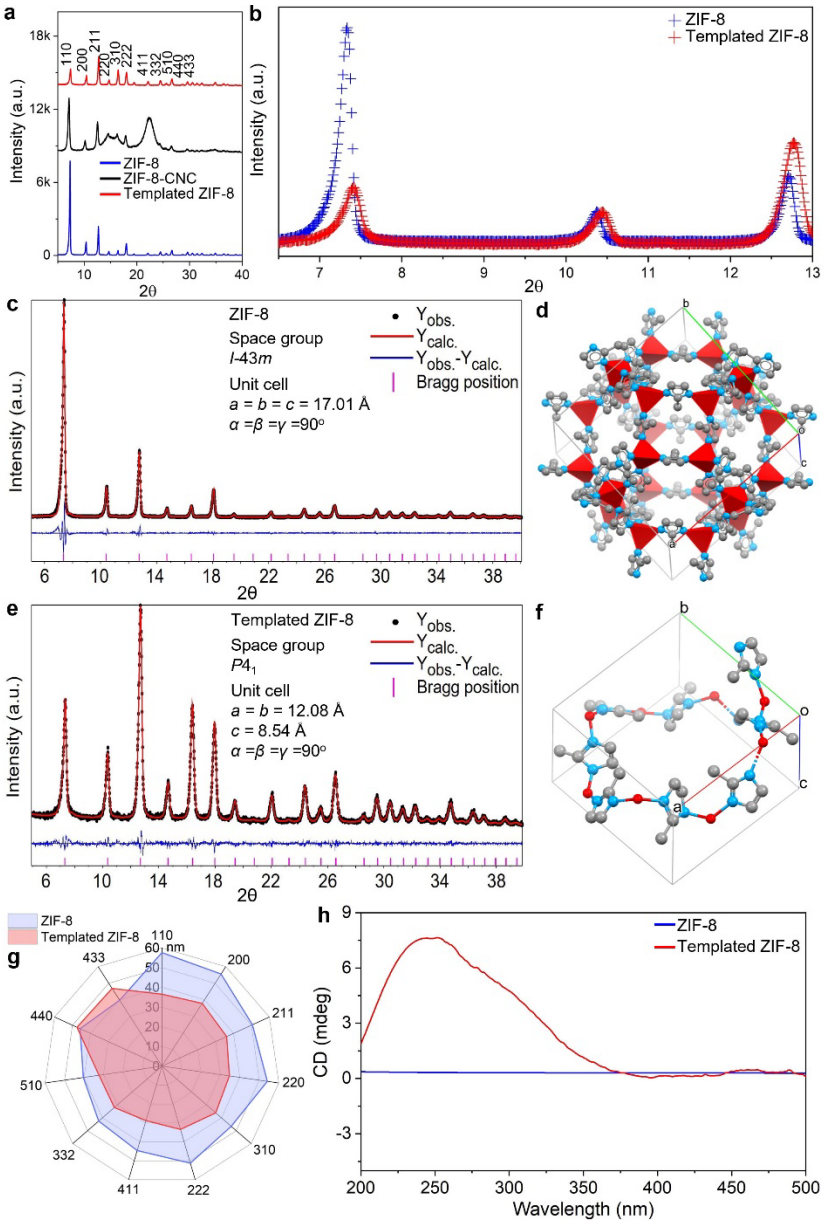

Figure 3. Crystal structure and chirality of templated-grown ZIF-8. a) XRD of ZIF-8, ZIF-8-CNC, and templated ZIF-8, respectively. b) Major XRD peaks of ZIF-8 and templated ZIF-8. Structural refinement of c) ZIF-8 and e) templated ZIF-8 from XRD analysis illustrating the observed pattern (black) and Rietveld refinement fitting (red). The blue lines display the difference between the observed XRD and Rietveld refinement. Bragg positions are shown by magenta ticks. d, f) The corresponding unit cells of the ZIF-8 and templated ZIF-8, respectively. The structure model for ZIF-8 is adopted from the database, joint Cambridge Crystallographic Data Centre (CCDC) and Fachinformationszentrum (FIZ) Karlsruhe Access Structures service.[52] A new crystal structure, for chiral ZIF-8 suggested in this study, has been deposited with a joint CCDC and FIZ Karlsruhe Access Structures service.[53] g) Crystallite size of ZIF-8 and templated ZIF-8 for different planes. h) Circular dichroism (CD) spectra of ZIF-8 and templated ZIF-8.

Thus, the template-grown ZIF-8 no longer possesses a cubic unit cell but the transformed unit cell

is compressed in the c direction and overall unit cell volume shrinks to a great extent. Overall, this change gave rise to a new tetragonal symmetry.

Next, the Scherrer equation was applied to calculate the mean crystallite size of ZIF-8 crystals normal to the different crystal planes[54]:

$$D_{hkl} = \frac{K\lambda}{B\cos\theta} \quad \text{(Eq. 1)}$$

where D_{hkl} is the mean crystallite size normal to the *hkl* plane, $K = 0.9$ is the crystal shape factor, λ is the wavelength of the X-ray (1.54 Å), B is the full width at half maximum of the diffraction peak, and θ is the Bragg's diffraction angle. For ZIF-8, the effective crystallite sizes are very similar, within 50 to 60 nm for different planes, consistent with cubic unit cells and global shape of microscopic MOF crystals (Figure 3g).

Overall, limited sizes indicate the presence of local defects, such as vacancies, which interrupt the coherence without distorting the overall crystal shape within larger crystals as shown by TEM and SEM images (Figures 1f and S11b).[55] The effective crystallite sizes decrease dramatically to 30-40 nm along different directions indicating a higher concentration of defects due to the confinement conditions of ZIF-8 crystals grown within the CNC matrix and anisotropic character of growth (Figures 1, 3g, and S13). The original CNC films (with diameter of ~7.5 cm) utilized for ZIF-8 growth are uniform with pale blue color (Figure 4a). In contrast, the composite ZIF-8-CNC film is milky and pale green due to the light scattering from the ZIF-8-CNC particles (Figure 4b).

Next, CD spectrum of templated-grown ZIF-8 shows the positive CD peaks at 250 nm in contrast to common ZIF-8, which does not exhibit any chiroptical activity (Figure 3h).[56,57] This distinct circular polarization of light clearly demonstrates the chirality nature of the template grown ZIF-8 with the left-handed organization. We assume that the chirality is transferred to the templated-grown ZIF-8 from the CNC bundles formed in the filtration process.[58] Both, the intensity and the position of the CD peak are in agreement with those previously reported for chiral ZIF nanostructures.[59]

In order to check the long-term stability of templated-grown ZIF-8, we measured the CD spectrum of templated-grown ZIF-8 stored at room temperature, ~23 ºC, under ambient conditions for 400

days after extraction (Figure S14a). The CD spectrum of templated-grown ZIF-8 400 days after extraction still presents the positive CD peak at 250 nm. Furthermore, templated-grown ZIF-8s 400 days and 1 day after extraction all displayed a relatively high asymmetry g-factor (Figure S14).[60,61,62] The value of this factor of 0.2 x 10^{-3} that left-handed organization of templated-grown ZIF-8 has been preserved for 400 days, therefore, confirming excellent long-term stability. The CD spectrum of the composite ZIF-8-CNC film also displays a positive peak whose position is shifted to IR range, beyond the range of detection. This indicates preservation of the left-handed chiral organization with significantly increased pitch length due to MOF crystals infiltrated into packed cellulose nanocrystals (Figure 4c). Furthermore, chiral nematic organization within characteristic layered Bouligand morphology as confirmed by SEM images (Figures 4c and 2a).[25]

To further investigate the internal structure of the ZIF-8-CNC composites, small angle neutron scattering (SANS) was employed (Figure 4d).[63,64] The two-dimensional (2D) SANS profiles in Figures 4e to 4g were azimuthally averaged to obtain the 1D scattering curves shown in Figure 4h. Analysis of this data was conducted by using a combination of the power law ($I \propto q^{-D}$, where I is the neutron scattering intensity, q is the scattering vector, and D is the power law exponent) with shape functions (cylindrical shape function for pristine CNC and ZIF-8-CNC and spherical shape function for ZIF-8 are verified by microscopic studies discussed above).[65,66] The parameters of these models were selected after analyzing multiple fits with minimum fitting error and the ability to match the morphologies considering the known information on morphology, dimensions, and shapes (Figure 2d). Finally, the fitting of the data was restricted to $0.0065\ Å^{-1} < q < 0.25\ Å^{-1}$ to minimize the distortions in the highest- and lowest-end q-data that arise from inelastic scattering.[67]

The SANS from original ZIF-8 shows rapid decay, following q^{-4}, which is indicative of 3-D objects with smooth surfaces and sharp interfaces (Figure 4h).[68] Using a spherical form factor, a crystal radius of 526 ± 19 nm was obtained from SANS data, which is a good agreement with TEM and SEM images (Figures 2d and S11b, respectively). Next, SANS data for the CNC films exhibited much lower power law exponents of 1.6 showing the formation and sparse mass fractals in the packed 1D cellulose nanocrystals instead of individual three-dimensional structures with sharp interfaces (Table S5).[68] Furthermore, an intermediate power law exponent of 2.7 for ZIF-8-CNC film indicates the formation of dense fractal structures resulting from interconnected morphologies as ZIF-8 nanocrystals are grown in between meshed 1D nanocrystals.[68,69]

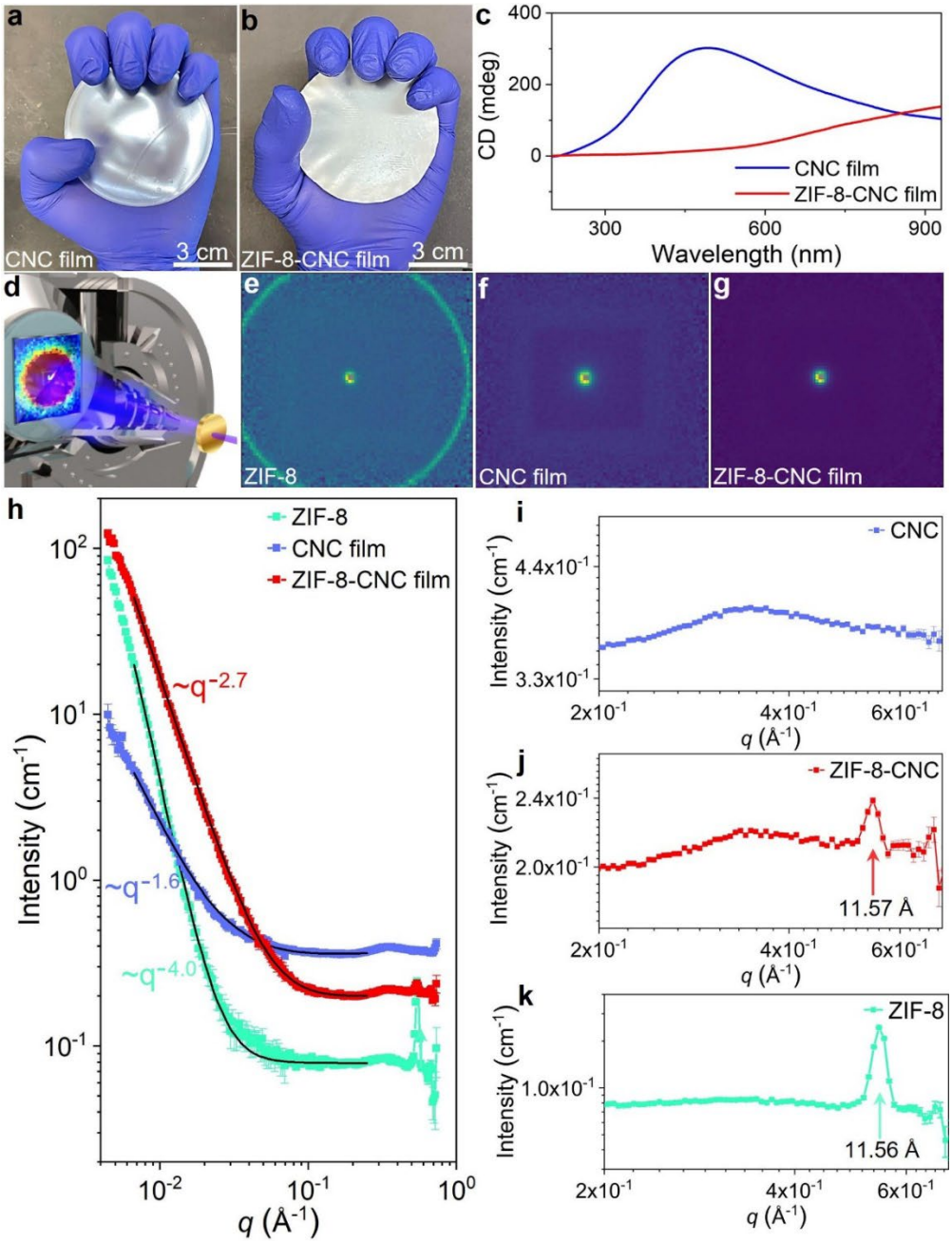

Figure 4. Structural analysis of the ZIF-8 and CNC materials. a,b) Photograph of hand-sized CNC film and ZIF-8-CNC film with ~7.5 cm diameter, respectively. c) CD spectrum of CNC film and ZIF-8-CNC film, respectively. d) Schematic diagram for SANS measurement of CNC and ZIF-8-CNC film. The direction of the neutron beam is perpendicular to the films. e-g) 2D SANS images (-0.50 $Å^{-1}<q_x<0.57$ $Å^{-1}$, -0.48 $Å^{-1}<q_y<0.45$ $Å^{-1}$) for ZIF-8, CNC film, and ZIF-8-CNC film, respectively. h) Radially averaged 1D SANS pattern (in logarithmic scale) of CNC film, ZIF-8, and ZIF-8-CNC. i-k) SANS profiles of CNC, ZIF-8-CNC, and ZIF-8, respectively.

Moreover, a dramatic increase in the effective radius was observed for the ZIF-8-CNC composite

compared to pristine CNC (21.0 ± 3.0 nm for ZIF-8-CNC vs. 2.0 ± 0.2 nm for CNC). Such an increase is consistent with microscopic observations and can be attributed to the growth of ZIF-8 crystals around the cellulose nanocrystals (Figures 2a, 2b, 2d, and 2e).

Finally, ZIF-8-CNC and ZIF-8 both exhibited an amorphous halo at lower q-values and a sharp peak in the highest achievable q-range at ~0.5 $Å^{-1}$ (Figures 4j and 4k). These scattering data are in contrast to only a broad amorphous halo from pure CNC film that indicated short-range ordering of nanocrystals within nematic monolayers (Figure 4i). In contrast, the presence of the sharp peaks in ZIF-8 based materials indicates the formation of crystalline phases. The d-spacing of ~11.6 Å ($2\cdot\pi/q_{peak}$) is close to the (110) Bragg reflection from the known unit cell of the ZIF-8 crystal but restricted resolution at high-q resolution precludes complete crystal structure analysis.

Overall, SANS and XRD studies suggest that distorted and anisotropic chiral ZIF-8 crystals have grown under confined spatial conditions in the organized helicoidal matrix: penetration of precursors within nanocellulose and integration with twisted amphiphilic nanocrystals leads to growth of chiral ZIF-8 crystal.

As known, ZIF-8 can be considered as prospective material for chemoresistive sensors with fast response/recovery times and high sensing sensitivity.[70] Next, we tested the ability of chiral ZIF-8 to differentiate chiral amino acids during absorption from solution on thin film electronic arrays, as a prototype of a prospective enantiotropic sensor.[11,71,72] To design enantiotropic sensing materials, the chiral ZIF-8 was used as an active layer that links channels with a width and length of 50 and 250 μm, respectively in thin-film transistor (Figure 5a). The current change in this sensing element, $\Delta I/I_o$, was measured after the chiral amino acids were adsorbed from solution onto the ZIF-8 channel,[73,74] where $\Delta I=I-I_o$ and I and I_o are the drain current when analyte is exposed to the sensor and baseline current, respectively.

In this study, we exploited the L-and D-alanine (Ala) for testing selective sensing (Figure 5a). As known, Ala is the most abundant amino acid in humans and the L-Ala enantiomer is involved in protein synthesis.[75,76] Additionally, L-Ala is used in pre- and post-operative nutrition therapy, along with other L-amino acids, and it is also employed as a precursor for pharmaceutical products.[77,78]

As we observed in our studies, the difference in current-voltage (I-V) data allows clear recognition

of L- and D-Ala amino acids (Figures 5b, 5c, and S15). Furthermore, multiple chemoresistive sensors responding to the different chirality of Ala molecules have been established to evaluate reliable chiral response. For this testing, we monitored the $\Delta I/I_o$ variation of the 30 chiral sensors array by statistical analysis (10 sensors per substrate, total three substrates were used, Figure S16 and S17). The results reflect the average $\Delta I/I_o$ values of the sensors with a standard deviation ranging from 10 to 30% in sensor-to-sensor variation ($\sigma/(\Delta I/I_o)$) of ~ 20 %) where σ is a standard deviation and $\Delta I/I_o$ is the average value of the 30-sensor array. As can be seen, traditional ZIF-8–based sensors display negligible chiral recognition by showing a negligible difference between $\Delta I_{L\text{-}Ala}/I_o$ and $\Delta I_{D\text{-}Ala}/I_o$ up to 400 μM (Figure 5d). On the contrary, the chiral ZIF-8 sensor demonstrates the clear difference between $\Delta I_{L\text{-}Ala}/I_o$ and $\Delta I_{D\text{-}Ala}/I_o$, indicating efficient sensing the chiral biomolecules even at a very small amount of a target analyte. Specifically, ~14.6, 42.9, 49.5, and 60.2 % increase in the current change are observed for D-Ala compared to the L-Ala at 50, 100, 200, and 400 μM concentrations, respectively.

The LOCD value which is critical for the recognition of enantiotropic molecules was about 300 μM as detected by comparing differential current ratios depending on D- and L-Ala analyte concentrations (Figure 5e). Moreover, the LOD value for chiral templated ZIF-8 was determined as 39 and 64 μM for D- and L-Ala analytes, respectively, based on absorption from the solution during drop-casting and current charge measurements.[79,80] It is important to note that the chiral-detection limit observed here is comparable or exceeds those for other traditional enantioselective sensors (Table S6). The electrical characteristic results of templated chiral ZIF-8 biosensors with varying chiral analytes concentration imply efficient enantioselective sensing properties occur due to the more favorable affinity of chiral ZIF-8 with D-Ala than L-Ala as shown in Figures 5f-i, associated with left-handedness of crystal structure of chiral ZIF-8.[81] We suggest that the chiral crystal structure of templated ZIF-8 provides more favorable interaction such as metal-coordinating[82] and H-bonding interactions[83] for right-handed chiral D-Ala molecules due to saturation of higher numbers of the interactions to left-handed ZIF-8 crystal structure due to shape-controlled complementary interactions (key-lock principle) (Figure 5f, h). Since Ala is capable of electron transfer,[84] induced dipole moment increases as interaction between Ala and ZIF-8 increases,[85,86] therefore increasing the current density within porous matrix as detected with I-V data at different concentrations.

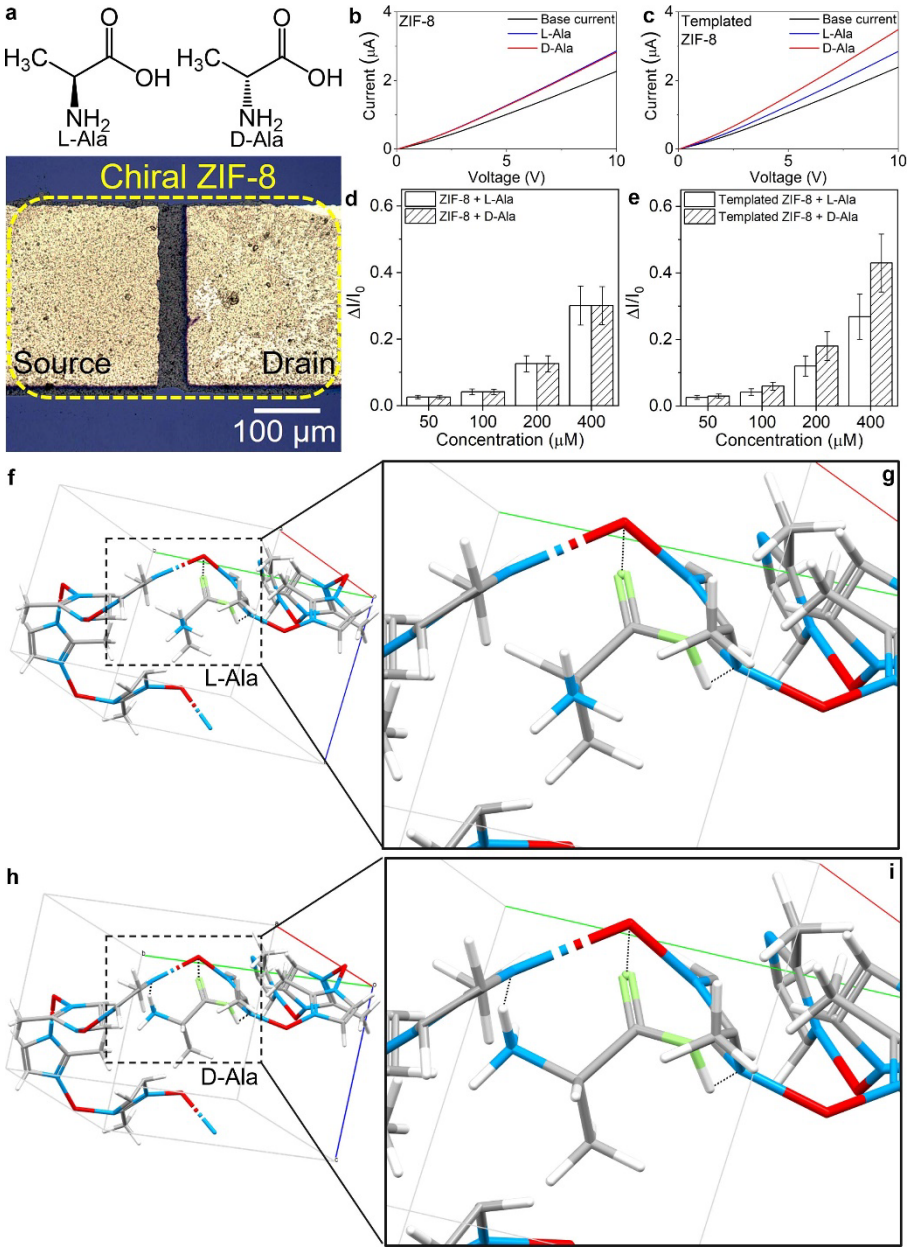

Figure 5. Templated chiral ZIF-8 enantioselective chemoresistive sensor proof of concept. a) Chemical structure of L-Ala and D-Ala (top panel). The configuration of the developed enantioselective sensors. Chiral ZIF-8 is deposited onto pre-patterned Au/Ti electrodes with channel width and length of 50 and 250 µm, respectively (bottom panel). Typical *I-V* curve of b) ZIF-8 and c) templated ZIF-8 to L-Ala and D-Ala at 400 µM, respectively. Current change ($\Delta I/I_o$) plot of d) ZIF-8 and e) templated ZIF-8 with respect to different concentrations of L- and D-Ala from 50 to 400 µM. Enantioselective interaction of templated ZIF-8 with f, g) L-Ala and h, i) D-Ala. D-Ala shows favorable interactions with templated ZIF-8 than L-Ala. Green: oxygen, blue: nitrogen, red: zinc, grey: carbon, and white: hydrogen.

It has been well known that the interaction between the metal atom and organic molecule can be directly confirmed using electrical and/or voltammetry.[87,88] Thus, observed different I-V curve of

chiral ZIF-8 toward L- and D-Ala directly confirms the enantioselective interaction of chiral ZIF-8 toward L- and D-Ala as illustrated in Figures 5b, 5c, and S15. The specific bonding types could be further studied using computational methods including molecular dynamics simulations for further studies.[89]

Conclusion

This work demonstrates that chiral ZIF-8 structures can be synthesized on twisted nano-templates with the left-handed helical motif (Figure S18) by growing ZIF-8 from achiral precursors in chiral nematic bio-templates with the helical supramolecular organization. The resulting chiral template-grown ZIF-8 crystals possess a tetragonal unit cell, which is clearly distinct from the conventional ZIF-8 cubic unit cell. Additionally, it exhibits a high (828 m^2/g) specific surface area that includes nanopores ($d < 2$ nm) and a greatly extended fraction of mesoporous open volume ($2 < d < 50$ nm). Chiral ZIF-8 enables facile sensing and recognition of amino acid enantiomers, being an active channel in the form of an enantioselective chemoresistive sensor with performance that exceeds common spectroscopic and electrochemical sensing abilities. It has been systemically investigated that conventional achiral ZIF-8 can show high chemical stability to diverse organic solvents and exceptional thermal stability (up to 550 °C).[50] Thus, considering same chemical bonding structure of chiral ZIF-8 is same with conventional ZIF-8 (composed of Zn-N bonding), the stability chiral ZIF-8 toward the air, water, common solvents and thermal treatment may also excel along with potential recyclability in gas uptake. Indeed, it was reported that conventional ZIF-8 can show the outstanding recycling stability toward gas uptake/release with the gas uptake efficiency over 90%.[90] Besides, we further envision that chiral ZIF-8 may show the enantioselective gas uptake/release capability owed to the it's chirality[85]. Last, it is worth to note that seamless growing of chiral metal-organic materials within porous naturally twisted plant-based matrices can provide hints about answering one of the unresolved compelling questions, the origin of homochirality found in nature.[91] We suggest that twisted biopolymer materials from plants can induce assembly of chiral metal-organic assemblies from achiral precursors as a potential case for naturally occurring organic chirality.

For further exploration, the generality of this method for other MOFs can be explored by allowing the growth of achiral precursors of MOFs on twisted nano-templates. Potential candidates include i) achiral indium nitrate pentahydrate, zinc nitrate tetrahydrate, and imidazole for chiral ZIF-5

synthesis and ii) achiral cobalt nitrate hexahydrate and benzimidazole for chiral ZIF-9 synthesis using CNC as chiral bio-template. We envision that if chiral bio-templates can universally transfer chirality to diverse achiral precursors of MOFs, this can facilitate scalability in making chiral MOFs by replacing traditionally employed synthetic chiral reagents. Moreover, we suggest that this approach can be expanded by exploring if these templated chiral MOFs can be utilized as a stable secondary template for growing chiral inorganic nanostructures.

Supporting Information

Supporting Information is available from the Wiley Online Library or from the author.

Acknowledgments

We would like to thank Dr. J. Leisen for performing ^{13}C CP/MAS NMR and Dr. A. Balzer and Dr. N. Stingelin for help with TGA.

Funding: This work is supported by Air Force Office for Scientific Research grant FA9550-20-1-0305 and a grant from the South Korea National Research Foundation (NRF) (MSIT:2021R1A6A3A14039290). A portion of this research used resources at the Spallation Neutron Source, a DOE Office of Science User Facility operated by the ORNL.

Conflict of Interest: The authors declare no conflict of interest.

Author contributions: M.K. and V.V.T. conceived and designed this research. M.K., H.L., and M.L.B. synthesized ZIF-CNC. M.K. extracted templated ZIF-8 from CNC-MOF. H.L. and M.L.B. synthesized control ZIF-8. M.K. performed XRD analysis and K.M.A. conducted XRD measurements. M.K. performed CD measurement and analysis. H.L. collected TGA data and M.K. performed analysis. M.K. conducted the NMR analysis. H.L. and D.B. performed HR-SEM, EDX, and AFM measurements and M.K. conducted the analysis. H.L. and K.J.P conducted HR-TEM measurements. P.F. analyzed the SANS data. W.T.H performed SANS measurements and helped SANS analysis. Y.Y. conducted BET measurements and analysis. M.K. conceived the application of templated ZIF-8 to enantioselective sensing electronic devices and M.J.H. fabricated

enantioselective sensing electronic devices and electrical measurements and M.K. and M.J.H conducted analysis. M.K. conducted all ATR-FT-IR with help of Jiwoo Yu and the analysis. H.L. and K.J.P. measured the XPS spectra of samples. P.F. analyzed XPS data. S.S. provided critical review, comments, and helpful discussions. Manuscript writing was led and conducted by M.K. and edited by V.V.T. All authors offered critical input to the writing of the paper.

Data Availability Statement: All data needed to evaluate the conclusions in the paper are present in the paper and/or the Supplementary Materials.

Keywords: *Chiral bio-templates, chiral metal-organic frameworks, enantioselective chemoresistive sensors*

References

[1] W. Xue, C. D. Sewell, Q. Zhou, Z. Lin, *Angew. Chem. Int. Ed.* **2022**, *134*, e202206512.
[2] A. Knebel, B. Geppert, K. Volgmann, D. I. Kolokolov, A. G. Stepanov, J. Twiefel, P. Heitjans, D. Volkmer, J. Caro, *Science* **2017**, *358*, 347-351.
[3] F. Carraro, J. D. Williams, M. Linares-Moreau, C. Parise, W. Liang, H. Amenitsch, C. Doonan, C. O. Kappe, P. Falcaro, *Angew.Chem.* **2020**, *132*, 8200-8204.
[4] C. Wang, G. Sudlow, Z. Wang, S. Cao, Q. Jiang, A. Neiner, J. J. Morrissey, E. D. Kharasch, S. Achilefu, S. Singamaneni, *Adv. Healthc. Mater.* **2018**, *7*, 1800950.
[5] R. A. Perlata, M. T. Huxley, Z. Shi, Y.-B. Zhang, C. J. Sumby, C. J. Doonan, *Chem. Commun.* **2020**, *56*, 15313-15316.
[6] C. Herbert, S. S. Abeyrathna, N. S. Abeyrathna, Y. H. Wijesundara, O. R. Brohlin, F. Carraro, H. Amenitsch, P. Falcaro, M. A. Luzuriaga, A. Durand-Silva, S. D. Diwakara, R. A. Smaldone, G. Meloni, J. J. Gassensmith, *Nat. Commun.* **2021**, *12*, 2202.
[7] Z. Chen, M. R. Mian, S.-J. Lee, H. Chen, X. Zhang, K. O. Kirlikovali, S. Shulda, P. Melix, A. S. Rosen, P. A. Parilla, T. Gennett, R. Q. Snurr, T. Islamoglu, T. Yildirim, O. K. Farha, *J. Am. Chem. Soc.* **2021**, *143*, 18838-18843.
[8] S.-H. Yang, R. Naaman, Y. Paltiel, S. S. P. Parkin, *Nat. Rev. Phys.* **2021**, *3*, 328-343.
[9] M. Kim, V. V. Tsukruk, *Nat. Photon.* **2022**, *16*, 337-338.
[10] L. Pasteur, *Acad. Sci. Paris* **1848**, *26*, 535-538.
[11] B. Ni, H. Cölfen, *SmartMat* **2021**, *2*, 17-32.
[12] V. Sharma, M. Crne, J. O. Park, M. Srinivasarao, *Science* **2009**, *325*, 449-451.
[13] S. Kinoshita, S. Yoshioka, J. Miyazaki, *Rep. Prog. Phys.* **2008**, *71*, 076401.
[14] R. Xiong, J. Luan, S. Kang, C. Ye, S. Singamaneni, V. V. Tsukruk, *Chem. Soc. Rev.* **2020**, *49*, 983-1031.
[15] D. Kennedy, C. Norman, *Science* **2005**, *309*, 75.

[16] Z. Sharifzadeh, K. Berijani, A. Morsali, *Coord. Chem. Rev.* **2021**, *445*, 214083.
[17] R. E. Morris, X. Bu, *Nat. Chem.* **2010**, *2*, 353-361.
[18] Q.-Y. Liu, W.-L. Xiong, C.-M. Liu, Y.-L. Wang, J.-J. Wei, Z.-J. Xiahou, L.-H. Xiong, *Inorg. Chem.* **2013**, *52*, 6773-6775.
[19] W. Meng, S. Kondo, T. Ito, K. Komatsu, J. Pirillo, Y. Hijikata, Y. Ikuhara, T. Aida, H. Sato, *Nature* **2021**, *598*, 298-303.
[20] L. Tong, S. Huang, Y. Shen, S. Liu, X. Ma, F. Zhu, G. Chen, G. Ouyang, *Nat. Commun.* **2022**, *13*, 951.
[21] S. Huang, G. Chen, G. Ouyang, *Chem, Soc. Rev.* **2022**, *51*, 6824-6863.
[22] S. Liu, L. Han, Y. Duan, S. Asahina, O. Terasaki, Y. Cao, B. Liu, L. Ma, J. Zhang, S. Che, *Nat. Commun.* **2012**, *3*, 1215.
[23] J. J. Richardson, B. L. Tardy, J. Guo, K. Liang, O. J. Rojas, H. Ejima, *ACS Sustain. Chem. Eng.* **2019**, *7*, 6287-6294.
[24] X. Liu, Y. Xiao, Z. Zhang, Z. You, J. Li, D. Ma, B. Li, *Chin. J. Chem.* **2021**, *39*, 3462-3480.
[25] M. Kim, H. Lee, M. C. Krecker, D. Bukharina, D. Nepal, T. J. Bunning, V. V. Tsukruk, *Adv. Mater.* **2021**, *33*, 2103674.
[26] M. Giese, L. K. Blusch, M. K. Khan, M. J. MacLachlan, *Angew. Chem. Int. Ed.* **2015**, *54*, 2888-2910.
[27] M. Chekini, E. Prince, L. Zhao, H. Mundoor, I. I. Smalyukh, E. Kumacheva, *Adv. Opt. Mater.* **2020**, *8*, 1901911.
[28] T. O'brien, L. Crocker, R. Thompson, K. Thompson, P. Toma, D. Conlon, B. Feibush, C. Moeder, G. Bicker, N. Grinberg, *Anal. Chem.* **1997**, *69*, 1999-2007.
[29] M. Schlesinger, M. Giese, L. K. Blusch, W. Y. Hamad, M. J. MacLachlan, *Chem. Commun.* **2015**, *51*, 530-533.
[30] C. M. Walters, K. R. Adair, W. Y. Hamad, M. J. MacLachlan, *Eur. J. Inorg. Chem.* **2020**, *2020*, 3937-3943.
[31] H. Qi, K. E. Shopsowitz, W. Y. Hamad, M. J. MacLachlan, *J. Am. Chem. Soc.* **2011**, *133*, 3728-3731.
[32] J. Zhang, S. Chen, R. A. Nieto, T. Wu, P. Feng, X. Bu, *Angew. Chem. Int. Ed.* **2010**, *49*, 1267-1270.
[33] Y. Kang, S. Chen, F. Wang, J. Zhang, X. Bu, *Chem. Commun.* **2011**, *47*, 4950-4952.
[34] J. Zhang, S. Chen, T. Wu, P. Feng, X. Bu, *J. Am. Chem. Soc.* **2008**, *130*, 12882-12883.
[35] L. Lei, F. Pan, A. Lindbråthen, X. Zhang, M. Hillestad, Y. Nie, L. Bai, X. He, M. D. Guiver, *Nat. Commun.* **2021**, *12*, 268.
[36] H. Wang, G. Gurau, R. D. Rogers, *Chem. Soc. Rev.* **2012**, *41*, 1519-1537.
[37] A. S. Spitsyna, A. S. Poryvaev, N. E. Sannikova, A. A. Yazikova, I. A. Kirilyuk, S. A. Dobrynin, O. A. Chinak, M. V. Fedin, O. A. Krumkacheva, *Molecules* **2022**, *27*, 3240.
[38] Y. Zhang, Y. Jia, M. Li, L. a. Hou, *Sci. Rep.* **2018**, *8*, 9597.
[39] L. T. Kuhn, K. Motiram-Corral, T. J. Athersuch, T. Parella, M. Pérez-Trujillo, *Angew. Chem. Int. Ed.* **2020**, *59*, 23615-23619.
[40] M. Pérez-Trujillo, E. Monteagudo, T. Parella, *Anal. Chem.* **2013**, *85*, 10887-10894.
[41] H. T. Kwon, H.-K. Jeong, A. S. Lee, H. S. An, J. S. Lee, *J. Am. Chem. Soc.* **2015**, *137*, 12304-12311.
[42] K. E. Shopsowitz, W. Y. Hamad, M. J. MacLachlan, *J. Am. Chem. Soc.* **2012**, *134*, 867-870.
[43] A. Alanis, J. H. Valdés, N.-V. María Guadalupe, R. Lopez, R. Mendoza, A. P. Mathew, R. Díaz de León, L. Valencia, *RSC Adv.* **2019**, *9*, 17417-17424.
[44] R. L. Papurello, L. A. Lozano, E. V. Ramos-Fernández, J. L. Fernández, J. M. Zamaro, *ChemPhysChem* **2019**, *20*, 3201-3209.
[45] S. Gadipelli, W. Travis, W. Zhou, Z. Guo, *Energy Environ. Sci.* **2014**, *7*, 2232-2238.
[46] K. Adstedt, E. A. Popenov, K. J. Pierce, R. Xiong, R. Geryak, V. Cherpak, D. Nepal, T. J. Bunning, V.

V. Tsukruk, *Adv. Funct. Mater.* **2020**, *30*, 2003597.
[47] V. F. Korolovych, V. Cherpak, D. Nepal, A. Ng, N. R. Shaikh, A. Grant, R. Xiong, T. J. Bunning, V. V. Tsukruk, *Polymer* **2018**, *145*, 334-347.
[48] Y. Nishiyama, P. Langan, H. Chanzy, *J. Am. Chem. Soc.* **2002**, *124*, 9074-9082.
[49] C. Avci, I. Imaz, A. Carné-Sánchez, J. A. Pariente, N. Tasios, J. Pérez-Carvajal, M. I. Alonso, A. Blanco, M. Dijkstra, C. López, D. Maspoch, *Nat. Chem.* **2018**, *10*, 78-84.
[50] K. S. Park, Z. Ni, A. P. Côté, J. Y. Choi, R. Huang, F. J. Uribe-Romo, H. K. Chae, M. O'Keeffe, O. M. Yaghi, *Proc. Natl. Acad. Sci.* **2006**, *103*, 10186-10191.
[51] B. Tiţa, A. Fuliaş, G. Bandur, E. Marian, D. Tiţa, *J. Pharm. Biomed. Anal.* **2011**, *56*, 221-227.
[52] CCDC deposition number: 866423.
[53] CCDC deposition number: 2264401.
[54] U. Holzwarth, N. Gibson, *Nat. Nanotechnol.* **2011**, *6*, 534.
[55] M. Rudolph, M. Motylenko, D. Rafaja, *IUCrJ* **2019**, *6*, 116-127.
[56] A. Matsumoto, H. Ozaki, S. Tsuchiya, T. Asahi, M. Lahav, T. Kawasaki, K. Soai, *Org. Biomol. Chem.* **2019**, *17*, 4200-4203.
[57] B.-Q. Song, D.-Q. Chen, Z. Ji, J. Tang, X.-L. Wang, H.-Y. Zang, Z.-M. Su, *Chem. Commun.* **2017**, *53*, 1892-1895.
[58] T. G. Parton, R. M. Parker, G. T. van de Kerkhof, A. Narkevicius, J. S. Haataja, B. Frka-Petesic, S. Vignolini, *Nat. Commun.* **2022**, *13*, 2657.
[59] T. Zhao, J. Han, X. Jin, Y. Liu, M. Liu, P. Duan, *Angew. Chem. Int. Ed.* **2019**, *58*, 4978-4982.
[60] S. C. Gad, Pharmaceutical sciences encyclopedia: drug discovery, development, and manufacturing, John Wiley & Sons, **2010**.
[61] W. Feng, J.-Y. Kim, X. Wang, H. A. Calcaterra, Z. Qu, L. Meshi, N. A. Kotov, *Sci. Adv.* **2017**, *3*, e1601159.
[62] D. Qu, H. Zheng, H. Jiang, Y. Xu, Z. Tang, *Adv. Opt. Mater.* **2019**, *7*, 1801395.
[63] L. He, L. Yang, M. Dincă, R. Zhang, J. Li, *Angew. Chem. Int. Ed.* **2020**, *59*, 9773-9779.
[64] J. Van Rie, G. González-Rubio, S. Kumar, C. Schütz, J. Kohlbrecher, M. Vanroelen, T. Van Gerven, O. Deschaume, C. Bartic, L. M. Liz-Marzán, *Chem. Commun.* **2020**, *56*, 13001-13004.
[65] C. Schütz, M. Agthe, A. B. Fall, K. Gordeyeva, V. Guccini, M. Salajková, T. S. Plivelic, J. P. F. Lagerwall, G. Salazar-Alvarez, L. Bergström, *Langmuir* **2015**, *31*, 6507-6513.
[66] J. Cravillon, R. Nayuk, S. Springer, A. Feldhoff, K. Huber, M. Wiebcke, *Chem. Mater.* **2011**, *23*, 2130-2141.
[67] C. Do, W. T. Heller, C. Stanley, F. X. Gallmeier, M. Doucet, G. S. Smith, *Nucl. Instrum. Methods Phys. Res., Sect. A* **2014**, *737*, 42-46.
[68] Y. Ren, X. Zuo, *Small Methods* **2018**, *2*, 1800064.
[69] J. S. Pedersen, *Adv. Colloid Interface Sci.* **1997**, *70*, 171-210.
[70] M. Zhan, S. Hussain, T. S. AlGarni, S. Shah, J. Liu, X. Zhang, A. Ahmad, M. S. Javed, G. Qiao, G. Liu, *Mater. Res. Bull.* **2021**, *136*, 111133.
[71] H. V. T. Nguyen, Y. Jiang, S. Mohapatra, W. Wang, J. C. Barnes, N. J. Oldenhuis, K. K. Chen, S. Axelrod, Z. Huang, Q. Chen, M. R. Golder, K. Young, D. Suvlu, Y. Shen, A. P. Willard, M. J. A. Hore, R. Gómez-Bombarelli, J. A. Johnson, *Nat. Chem.* **2022**, *14*, 85-93.
[72] W. H Brooks, W. C Guida, K. G Daniel, *Curr. Trends Med. Chem.* **2011**, *11*, 760-770.
[73] J. Peng, Z. Zhang, C. Hu, Z. Wang, Y. Kang, W. Chen, T. Ao, *J. Sol-Gel Sci. Technol.* **2021**, *99*, 339-353.

[74] E. M. Mahdi, J.-C. Tan, *Polymer* **2016**, *97*, 31-43.
[75] F. Temel, S. Erdemir, B. Tabakci, M. Akpinar, M. Tabakci, *Anal. Bioanal. Chem.* **2019**, *411*, 2675-2685.
[76] Q. Zhao, J. Yang, J. Zhang, D. Wu, Y. Tao, Y. Kong, *Anal. Chem.* **2019**, *91*, 12546-12552.
[77] M. Ikeda, S. Takeno, in *Corynebacterium glutamicum*, Springer, **2013**, pp. 107-147.
[78] P. Hols, M. Kleerebezem, A. N. Schanck, T. Ferain, J. Hugenholtz, J. Delcour, W. M. de Vos, *Nat. Biotechnol.* **1999**, *17*, 588-592.
[79] G. Indrayanto, in *Profiles of Drug Substances, Excipients and Related Methodology, Vol. 43* (Ed.: H. G. Brittain), Academic Press, **2018**, pp. 359-392.
[80] N. Patel, P. Shukla, P. Lama, S. Das, T. K. Pal, *Cryst. Growth Des.* **2022**, *22*, 3518-3564.
[81] Y.-W. Zhao, Y. Wang, X.-M. Zhang, *ACS Appl. Mater. Interfaces* **2017**, *9*, 20991-20999.
[82] V. Nozari, C. Calahoo, J. M. Tuffnell, D. A. Keen, T. D. Bennett, L. Wondraczek, *Nat. Commun.* **2021**, *12*, 5703.
[83] J. Li, B. Liu, X. Zhang, D. Cao, G. Chen, *J. Phys. Chem. C* . **2017**, *121*, 25347-25352.
[84] S. Rodríguez, L. Makinistian, E. Albanesi, *Appl. Surf. Sci.* **2017**, *419*, 540-545.
[85] X. Shang, C. H. Park, G. Y. Jung, S. K. Kwak, J. H. Oh, *ACS Appl. Mater. Interfaces* **2018**, *10*, 36194-36201.
[86] R. S. Mulliken, *J. Chem. Phys.* **1955**, *23*, 1841-1846.
[87] M. Aslanoglu, C. J. Isaac, A. Houlton, B. R. Horrocks, *Analyst* **2000**, *125*, 1791-1798.
[88] R. K. Boggess, D. A. Zatko, *J. Chem. Educ.* **1975**, *52*, 649.
[89] S. Cruz-León, N. Schwierz, *Langmuir* **2020**, *36*, 5979-5989.
[90] Y. Yu, L. Ren, M. Liu, S. Huang, X. Xiao, R. Liu, L. Wang, W. Xu, *ACS Appl. Mater. Interfaces* **2019**, *11*, 31291-31301.
[91] A. Xin, Y. Su, S. Feng, M. Yan, K. Yu, Z. Feng, K. Hoon Lee, L. Sun, Q. Wang, *Adv. Mater.* **2021**, *33*, 2006946.

For Table of Contents

A novel class of chiral metal-organic frameworks (MOFs) is generally obtained through complex synthetic routes by using a limited choice of reactive chiral organic precursors as the primary linkers or auxiliary ligands. We report a facile synthesis of chiral MOFs, specifically, zeolitic imidazolate framework-8 (ZIF-8), from achiral precursors grown on chiral nematic cellulose-derived nanostructured bio-templates. The template-grown chiral ZIF-8 possesses a tetragonal crystal structure with a chiral space group of $P4_1$, which is different from a traditional cubic crystal structure of $I\text{-}43m$ for freely grown conventional ZIF-8. The chiral structure demonstrates enantioselective recognition and chiral sensing abilities with a low limit of detection of 39 μM and the corresponding limit of chiral detection of 300 μM for representative chiral amino acid, D- and L- alanine."